JGR Solid Earth

The Importance of the Inelastic and Elastic Structures of the Crust in Constraining Glacial Density, Mass Change, and Isostatic Adjustment From Geodetic Observations in Southeast Alaska

William Durkin[1] [ID] **, Samuel Kachuck[2,3]** [ID] **, and Matthew Pritchard[1]** [ID]

[1]Earth and Atmospheric Sciences Department, Cornell University, Ithaca, NY, USA, [2]Department of Physics, Cornell University, Ithaca, NY, USA, [3]Department of Climate and Space Science and Engineering, University of Michigan, Ann Arbor, MI, USA

Abstract Elastic deformation of the solid Earth in response to ice mass loss offers a promising constraint on the density of glacial material lost. Further, the elastic response to modern deglaciation is important to constrain for studies of glacial isostatic adjustment to determine the mantle's structure and rheology. Models of this elastic uplift are commonly based on the 1-D, seismically derived global average Preliminary Reference Earth Model and typically neglect uncertainties that can arise from regional differences in elastic structure from that of the global average, lateral heterogeneities within the region, and inelastic behavior of the crust. We quantify these uncertainties using an ensemble of 1-D local elastic structure models and empirical relations for the effects of inelasticity in the upper ~10 km of the crust. In Southeast Alaska, modeling elastic uplift rates with local elastic structures results in up to a 20–40% difference from those modeled with the Preliminary Reference Earth Model. Although these differences are limited to regions near to ice-covered areas, they are comparable to the differences in uplift rates expected from the loss of firn versus loss of ice. Far from ice-covered areas, where most of the region's GPS observations were made, these differences become insignificant and do not affect previous glacial isostatic adjustment studies in the region. The methods presented here are based on the globally available LITHO1.0 seismic model and open source software, and the approach of using an ensemble of 1-D elastic structures can be easily adapted to other regions around the world.

1. Introduction

Glaciers, icefields, and ice sheets across the world can gain and lose several to hundreds of gigatonnes of mass on seasonal and annual time scales (e.g., Gardner et al., 2013; Luthcke et al., 2013; Shepherd et al., 2018), evoking a linear, elastic response from the solid Earth at rates on the scale of millimeters to centimeters per year (e.g., Compton et al., 2017; Khan et al., 2007; Larsen et al., 2005). Geodetic observations of this elastic deformation may be used to investigate rates of deglaciation (e.g., Zhao et al., 2014), dynamic glacier processes (e.g., Adhikari et al., 2017; Bevan et al., 2015), and the rheological structure of the Earth's interior (e.g., Auriac et al., 2013).

When widespread deglaciation occurs at decadal to centennial time scales in regions underlain by a low viscosity asthenosphere (10^{18}–10^{19} Pa s), such as in Iceland (Auriac et al., 2013), Patagonia (Lange et al., 2014), Southeast Alaska (Larsen et al., 2005), and regions of West Antarctica (Barletta et al., 2018; Nield et al., 2014), the elastic deformation is superimposed on to deformation caused by the viscous relaxation of the mantle (i.e., glacial isostatic adjustment or GIA). Once the elastic component is identified and constrained, the viscous deformation may be used to infer rheological parameters of the solid Earth such as the elastic thickness of the lithosphere and viscosity of the mantle, which can be difficult to constrain through other geophysical techniques. Further, these regions have other deformation processes occurring, for example, tectonic (e.g., Elliott et al., 2010; Sauber & Molnia, 2004), magmatic (e.g., Spaans et al., 2015), and hydrologic loading (e.g., Drouin et al., 2016). Constraining the elastic deformation from deglaciation is critical for partitioning the observed deformation field into these other sources of deformation.

In regions where continuous crustal deformation time series are available, long-term viscous deformation may sometimes be separated from the instantaneous elastic response to ice mass changes by carefully removing long-term trends from higher frequency changes (e.g., Wahr et al., 2013). However, in regions with high rates of GIA where the viscous response times are decadal to centennial (e.g., Barletta et al., 2018) or in regions with accelerating ice loss (e.g., Compton et al., 2015; Khan et al., 2007), it can be difficult to distinguish between the elastic and viscous components of deformation in this way. Often, GIA is inferred by first modeling the elastic deformation resulting from contemporary deglaciation using estimates of ice mass balance to load a half-space or a spherical, layered Earth and removing this model from observations of the total uplift, leaving the viscous component of deformation as the residual (e.g., Lange et al., 2014; Sato et al., 2011).

The propagation of biases and uncertainties in ice mass balance estimates used to model elastic deformation can directly impact the viscous deformation that is inferred. For example, in Southeast Alaska, Larsen et al. (2005) estimated that 20% of the uplift observed can be described by the elastic response to the average ice loss between the mid-1950s and mid-1990s, with a mean date in the 1970s (Arendt et al., 2002). Using updated ice-thinning rates with mean dates in the mid-1980s (Larsen et al., 2007), Sato et al. (2011) found that modeled elastic uplift could account for ∼26% of the total uplift and result in a ∼1.5× increase in the estimate of asthenospheric viscosity. However, ice thinning rates estimated by Larsen et al. (2007) are derived from an elevation time series in which the latest elevations come from an undercorrected Shuttle Radar Topography (SRTM) digital elevation model (DEM), resulting in overly negative mass loss rates (Berthier et al., 2018), and elastic uplift rates modeled using this time series (e.g., Sato et al., 2011) may similarly be overestimated. Moreover, while Sato et al. (2011) used ice-thinning rates with median dates in the mid-1980s to model the elastic uplift occurring during the period, GPS observations were made during the years 1996–2006 (mean epoch of 2003.5), ideally, the ice-thinning rates should be coterminous with the period of observation. Reducing the propagation of biases in ice mass balance estimates and improved alignment with deformation observations could help to better resolve other, larger uncertainties in constraining mantle rheology, such as the history of prior ice loss (e.g., Nield et al., 2016) and the constitutive equations describing mantle rheology (e.g., Steffen & Wu, 2011).

Uncertainties and biases associated with the Earth model used when estimating elastic deformation could also impact both glaciological investigations and inferred GIA deformation but have had less investigation. In studies of ice mass balance and regional GIA, a common choice for the elastic Earth model is the radially symmetric, seismically derived, global average Preliminary Reference Earth Model (PREM; Dziewonski & Anderson, 1981). Recently, Drouin et al. (2016) and Compton et al. (2017) found that to match modeled elastic deformation of seasonal mass changes of Icelandic icecaps with observed uplift required scaling the elastic response calculated using PREM by a factor of ∼2, calling into question the appropriateness of using the globally averaged elastic structure to represent a volcanic region such as Iceland. Centers of regional GIA and contemporary deglaciation are typically mountainous aggregates of different geologic terrains, often volcanic, and may not be well represented by a single 1-D globally averaged model of elastic structure.

Site-specific elastic structures constrained by seismology may be used (e.g., Nielsen et al., 2013); however, crustal material may not behave as elastically under glacial loading as it does during seismic wave propagation. In the upper ∼10 km of the crust, where low confining pressures allow rocks to be porous and fractured, a range of inelastic processes dependent on the frequency and amplitude of strain can dissipate elastic energy (e.g., Cheng & Johnston, 1981; Tutuncu et al., 1998). The presence of fluids can relax shear stresses, and flow between pores and fractures of varying compliance can viscously dissipate strain energy as heat (e.g., Carcione et al., 2018). Inelastic processes may occur even in the absence of fluids, such as during the formation and propagation of intergranular and intragranular fractures as well as slip along fractures and grain boundaries (Brantut et al., 2013; Wong & Baud, 2012). At the periods (10^{-2}–10^{2} s) and amplitudes (10^{-5}) of strain characteristic of seismic wave propagation, these inelastic effects are small, and the upper crust is well approximated as a purely elastic medium. But at larger strain amplitudes applied at periods of ∼10^{3} s and longer, inelastic deformation has the effect of reducing the apparent elastic moduli of the material (e.g., Cheng & Johnston, 1981; P. Johnson & Rasolofosaon, 1996; Tutuncu et al., 1998). The attenuation of elastic strain energy in the presence of fluids can be described by various analytical models (e.g., Carcione et al., 2018); however, inelasticity in dry rocks remains difficult to describe due to the complex physical processes involved and strong dependence on lithology and environmental conditions (Brantut et al., 2013). A more common approach is to empirically relate a material's "dynamic" Young's modulus found acoustically to the

"static" Young's modulus derived from the stress-strain curves found from triaxial deformation experiments performed on rock samples (e.g., Ameen et al., 2009; King, 1983; Najibi et al., 2015). The static-dynamic ratios measured this way can be small (∼0.4; e.g., Cheng & Johnston, 1981). This introduces an additional source of uncertainty worth considering, particularly when modeling near-field elastic deformation which is sensitive to the rheology of the upper crust.

In an ideal scenario, these complex regions would be modeled using a site-specific, laterally variable, 3-D elastic structure. However, this is not practical at the time of writing as the regions' 3-D structures are not well constrained and modeling elastic uplift rates from such structures would be computationally expensive given their large areas and, presumably, small-scale variations. To test the sensitivity of elastic deformation from hydrologic loading to variations in the crust, Dill et al. (2015) modified the upper portion of PREM with an ensemble of crustal models (Tesauro et al., 2012). We adopt a similar approach and use the global seismic density and velocity model LITHO1.0 (Pasyanos et al., 2014) to construct an ensemble of 1-D models representing the variations of crustal structure within Southeast Alaska. We consider empirical static-dynamic relations to test the importance of considering inelasticity in the crust and model the elastic deformation using this ensemble to bound the uncertainties due to variations in crustal structure. In addition, we are able to use this opportunity to update the elastic thinning rates to more closely match the 1996–2006 observation time of the Southeast Alaska campaign GPS data set (Elliott et al., 2010). While the focus of this study is on Southeast Alaska, the use of the global LITHO1.0 model makes our approach easily adaptable to other regions around the world.

2. Study Area

The Stikine Icefield, Juneau Icefield, and Glacier Bay region (Figure 1) comprise an area of ∼17,000 km^2 or 20% of the total glaciated area of Alaska and neighboring Canada (Pfeffer et al., 2014). They are the southernmost glacier complexes in Alaska, and melt across all elevations has been observed during summer months at the Juneau and Stikine icefields (Ramage et al., 2000; Smith et al., 1997). Annual melt rates for the Juneau and Stikine icefields between years 2000 and 2016 were −0.68 ± 0.15 and −0.83 ± 0.12 m w.e. yr^{-1}, respectively (Berthier et al., 2018), similar to the average mass balance of all Alaskan glaciers between 1994 and 2015 (−0.94 ± 0.14 m w.e. yr^{-1}; Larsen et al., 2015), while that of the Glacier Bay region between 1995 and 2011 (−0.6 ± 0.1 m w.e.yr $^{-1}$; A. J. Johnson et al., 2013) was significantly less negative than the Alaska-wide average. This annual removal of several gigatonnes of mass across each of these glacier complexes elicits the elastic uplift of the solid Earth at rates up to 10 mm yr^{-1} (Sato et al., 2011). Viscous uplift rates of up to 10–20 mm yr^{-1} emanate from Glacier Bay in response to the collapse of the Glacier Bay Icefield, which spanned an area of 5×10^3 km^2, reached thicknesses of up to 1.5 km, and lost ∼3,500 Gt between the years 1770–1950 (Larsen et al., 2005). In contrast to Hudson Bay, where the GIA response to the collapse of the Laurentide Ice Sheet following the last glacial maximum (∼20,000 years ago) drives present day uplift rates of up to 10 mm yr^{-1} (e.g., Sella et al., 2007), the present day uplift rate in response to the collapse of the Cordilleran Ice Sheet following the last glacial maximum is more subdued, at 1–2 mm yr^{-1} (Larsen et al., 2005). Taken in aggregate, present day viscoelastic uplift rates peak at ∼30 mm yr^{-1} centered near Glacier Bay (Elliott et al., 2010; Larsen et al., 2005).

3. Data and Methods

3.1. Ice Mass Balance

We estimate ice mass balance using a weighted linear regression on a time series of stacked DEMs. These methods were developed by previous studies (e.g., Berthier et al., 2016; Melkonian et al., 2014; Nuimura et al., 2012; Wang & Kaääb, 2015; Willis et al., 2012), and only the general procedure is outlined here with greater explanation and discussion provided in Supporting Information S1 (Dehecq et al., 2016; Gardelle et al., 2012). We construct an ice-elevation time series composed of SRTM, ArcticDEM, and Advanced Spaceborne Thermal Emission and Reflection Radiometer (ASTER) DEMs. ASTER DEMs are downloaded premade by the National Aeronautics and Space Administration/United States Geological Survey-operated Land Process Distributive Active Archive Center (LDAAP), and cloudy images are manually removed. A total of 358 ASTER DEMs covers the study area, spanning July 2000–May 2017 with an average of 15 ASTER elevations covering each pixel. ArcticDEM strips were derived from ∼0.5-m resolution stereoscopic imagery from Digital Globe and made available through the National Science Foundation and National Geospatial Intelligence Agency as 2-m resolution DEMs using the Surface Extraction with TIN-based Search-space
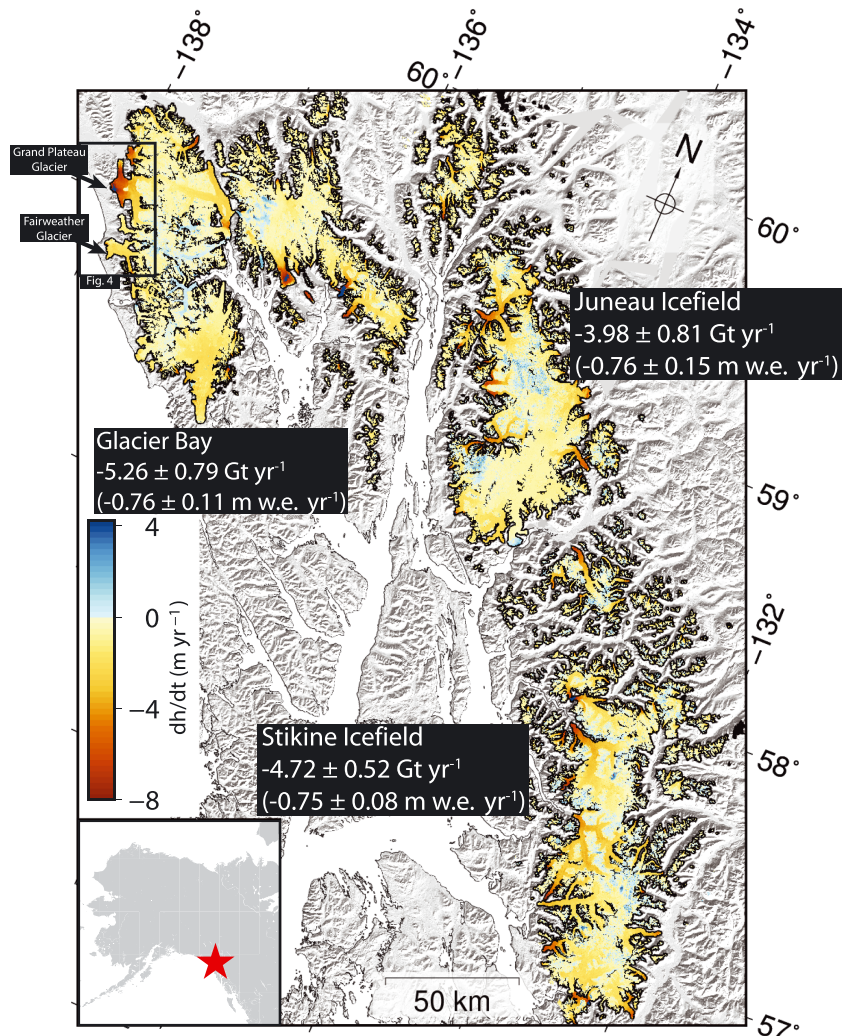
Figure 1. Ice thinning rates of the Stikine Icefield, Juneau Icefield, and Glacier Bay region estimated using the SRTM DEM, ArcticDEM, and Shuttle Radar Topography Mission digital elevation map spanning the years 2000–2017. The Shuttle Radar Topography Mission digital elevation map has been corrected for radar penetration into snow and ice (see Section S1.1). Mass balance estimates of the Stikine and Juneau icefields are updates of previous work by Melkonian et al. (2016) and Melkonian et al. (2014), respectively. The black box in the upper left corner outlines the region described in Figure 4.

Minimization method (https://www.pgc.umn.edu/data/arcticdem; Noh & Howat, 2015). ArcticDEM strips covering the study area total in 401 DEMs that span the time period October 2008–September 2016 with an average density of two ArcticDEM elevations per pixel. We downsample ArcticDEM strips to 30-m resolution and coregister both ArcticDEM and ASTER DEMs to off-ice pixels in the SRTM DEM using "PC_align" in the Ames Stereo Pipeline toolkit (Moratto et al., 2010). Off-ice pixels are identified using the Randolph Glacier Inventory version 5 (Pfeffer et al., 2014). Each DEM is assigned 1σ vertical uncertainty as the standard deviation between the off-ice pixels of it and the SRTM DEM. We estimate ice elevation change rates ($\frac{dh}{dt}$) using a linear regression on our elevation time series in which each elevation is weighted by the inverse of its uncertainty (e.g., Melkonian et al., 2014; Willis et al., 2012).

3.2. Elastic Uplift Rates, Inelasticity, and Uncertainties

We use an ensemble of seismic velocity models to quantify the uncertainty associated with representing a geologically variable region as a spherically symmetric model. This ensemble of models is based on LITHO1.0 (Pasyanos et al., 2014), a collection of seismically constrained estimates of density and P and S wave velocities that are globally available at 1° postings (Pasyanos et al., 2014). Each LITHO1.0 1-D profile has defined sublayers that include ice; water; between one and three sediment layers; an upper, middle,
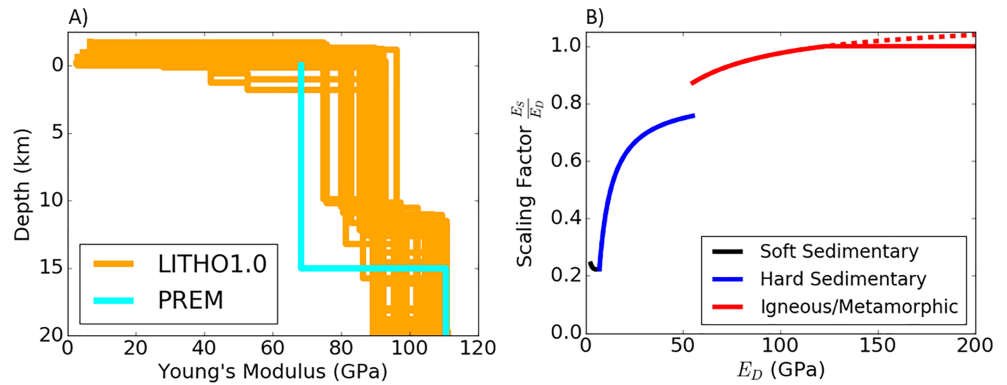
Figure 2. (a) Dynamic Young's moduli of the PREM global Earth model (cyan) and the ensemble of LITHO1.0 models used in this study (orange). LITHO1.0 profiles are sampled at a 1° spacing between 59–61° N and 130–139° W, with profiles sampling the ocean omitted. (b) Piecewise functions of the ratio of static and dynamic Young's moduli ($\frac{E_S}{E_D}$) as a function of the dynamic Young's modulus. Scaling functions for soft sedimentary (black), hard sedimentary (blue), and igneous/metamorphic (red) lithologies are from Yale and Swami (2017) and shown in equation (1). PREM = Preliminary Reference Earth Model.

and lower crust; and the lithospheric mantle. Excluding profiles that contain a water layer (i.e., profiles that are centered in the ocean), we consider 42 profiles between 59–61° N longitude and 130–139° W latitude (Figure 2a).

To estimate the effects of inelasticity in the upper crust to a first order, we use empirical relations fit by Yale and Swami (2017) to the static-dynamic ratios of Young's moduli (E_S/E_D) found from triaxial strain experiments of a combined 35 studies, described in equation (1). Many of the studies found in literature concerning correlations between E_S and E_D are conducted by the petroleum engineering community for the purpose of modeling the static response of hydrocarbon reservoirs. The triaxial strain experiments considered by Yale and Swami (2017) reflect these conditions. Confining pressures vary between 0 and 100 MPa (corresponding to depths of 0–5 km in the crust) and temperatures between 20 and 170 ° C. The impacts of confining pressure or the presence of fluids on the static-to-dynamic ratios are not controlled for, rather, static-to-dynamic ratios are separated by rock type. Yale and Swami (2017) found the following relations for soft sedimentary rocks (e.g., unconsolidated sands and shales), hard sedimentary rocks (e.g., tight sandstones, shales, and carbonates), and igneous/metamorphic rocks

$$E_S = \begin{cases} 5.796 \times 10^{-3} E_D{}^2 + 0.1587 E_D + 0.1756 & \text{soft sedimentary} \\ 0.8353 E_D - 4.283 & \text{hard sedimentary} \\ 1.1027 E_D - 12.639 & \text{igneous/metamorphic,} \end{cases} \qquad (1)$$

Table 1

Sublayer Structure of the LITHO1.0 Model and Range of Dynamic Young's Moduli (E_D) for the Ensemble of Elastic Structures

LITHO1.0 sublayer	E_D (GPa)	Yale and Swami (2017) lithology
Sedimentary layer 1	2.6–6.7	Soft sedimentary
Sedimentary layer 2	28.0–41.8	Hard sedimentary
Sedimentary layer 3	52.7–52.7	
Upper crust	74.8–96.2	Igneous/metamorphic
Middle crust	89.3–111.2	
Lower crust	111.2–138.0	
Lithospheric mantle	172.0–183.6	

Note. Each sublayer is assigned a lithologic classification from Yale and Swami (2017) for use with equation (1).
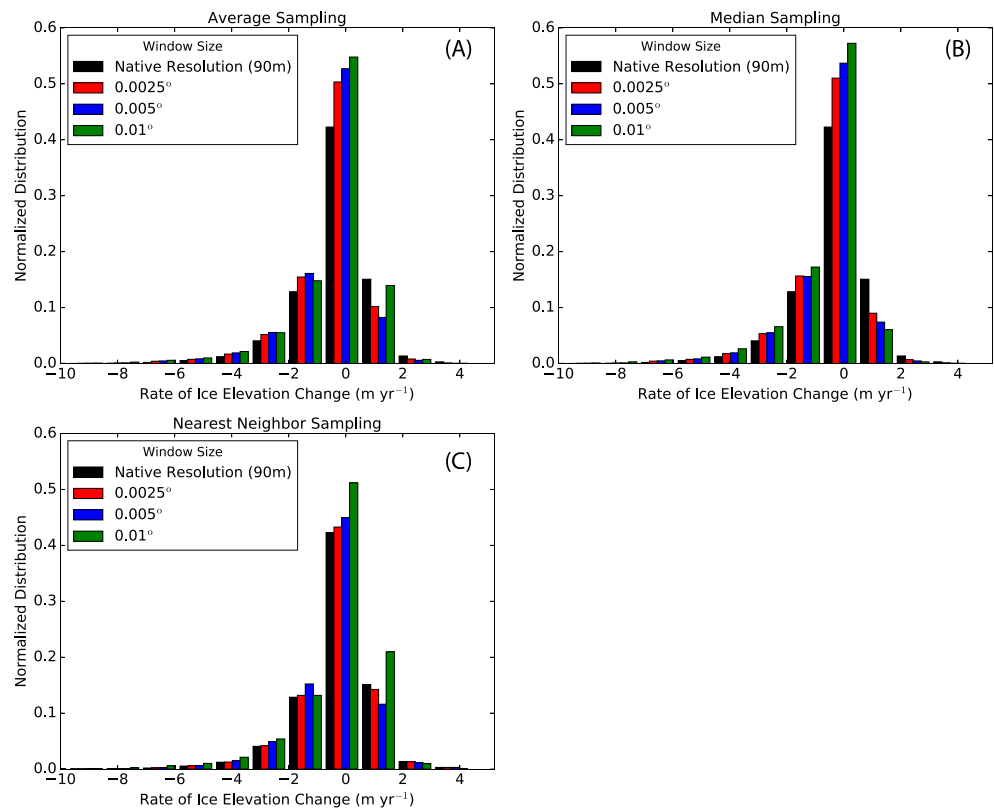
Figure 3. Histograms of $\frac{dh}{dt}$ sampled at 90 m, 0.0025°, 0.005°, and 0.01° resolutions under average (a), median (b), and nearest-neighbor (c) schemes. Median and averaging sampling methods show modest to no improvement in converging to the original $\frac{dh}{dt}$ distribution with increased resolution. Using the nearest neighbor method, $\frac{dh}{dt}$ distributions converge between sampling resolutions of 0.0025–0.005°.

where the demarcation between soft and hard sedimentary lithologies is defined by Yale and Swami (2017) as $E_S \approx 10$–15 GPa. Table 1 shows the minimum and maximum E_D of each LITHO1.0 sublayer for the ensemble of 42 profiles and its lithology classification for estimating E_S from equation (1). Figure 2b shows the ratio E_S/E_D estimated from Table 1 and equation (1). For $E_D > 123$ GPa, this ratio becomes greater than 1. This is a nonphysical and unexpected result, and we set the maximum E_S/E_D value to 1. The static bulk and static shear moduli are calculated from E_S, while the Poisson's ratio is unmodified.

As confining pressure increases, pores and fractures in rocks begin to close, decreasing the differences between the static and dynamic moduli (e.g., Asef & Najibi, 2013), and E_S has been observed to converge to E_D at depths of 10–15 km (Cheng & Johnston, 1981). The inelastic corrections in equation (1) are based on laboratory experiments conducted at a narrow range of confining pressures 0–100 MPa or the upper $\sim$5 km of the crust (Yale & Swami, 2017). We must take care that applying equation (1) to the LITHO1.0 ensemble does not yield static-dynamic ratios that are implausibly small at too great a depth. Figure S8 shows the scaling factor plotted against depth for each of the 42 LITHO1.0 structures. At a depth of 3.1 km, the smallest E_S/E_D in the ensemble is 0.75 - 0.90, and beyond depths of 10 km is no lower than 0.95. This is consistent with the E_S/E_D of 0.9 found by Cheng and Johnston (1981) for granite at confining pressures equivalent to depths of 12–13 km. Differences between the static and dynamic moduli of less than 5% at depths beyond 10 km are negligibly small for the purposes of this study.

Each of the elastic structures in our ensemble is used to describe a purely elastic Earth with radially symmetric material parameters. We use the open-source `giapy` (Kachuck, 2018) to calculate the load Love number solutions to the equations of motion for each of these models from the core-mantle boundary to the surface in response to the application of a spherical harmonic load, as described in Farrell (1972) and Cathles (1975). Load Love numbers computed using the elastic structure described by PREM using `giapy` match well with those calculated in Pan et al. (2015; Figure S5). Load Love numbers are calculated for each LITHO1.0-based
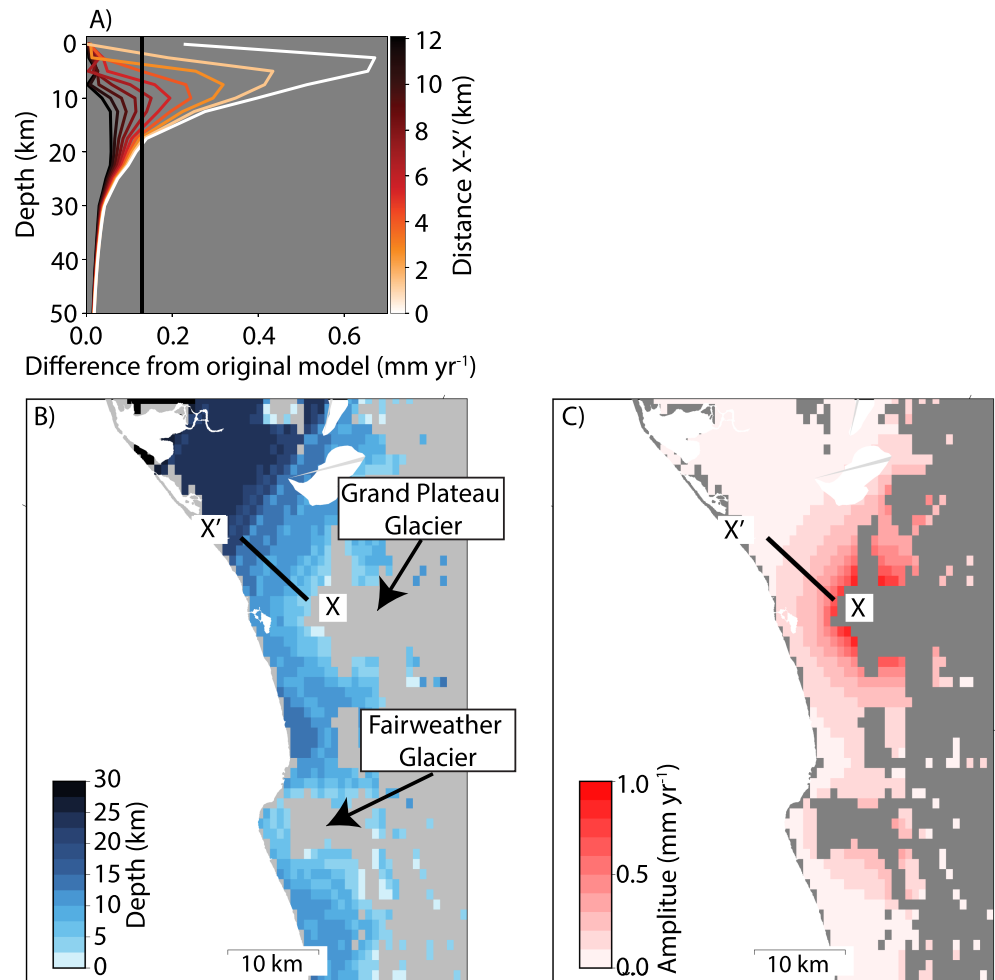
Figure 4. (a) Depth sensitivity to perturbations from PREM. The Young's modulus of PREM is reduced by a factor of 2 for 5-km-thick sublayers at various depths (y axis), and elastic uplift rates modeled from the perturbed structures are subtracted from those modeled using the original PREM (x axis). Sensitivity kernels are calculated along a 12-km X-X' transect (shown in (b) and (c)) with their distance along the transect shown by their color. Differences less than 5% of the average GPS uncertainty (0.13 mm yr^{-1}, black line) are considered insignificant. Sensitivity kernels are calculated at 0.1° postings for all off-ice areas in the study region, and the maximum difference and its associated depth are recorded. As an example, the depths and amplitudes of the peak differences are shown in (b) and (c), respectively, for the region surrounding the Grand Plateau and Fairweather glaciers (see boxed region in Figure 1). PREM = Preliminary Reference Earth Model.

elastic structure to a harmonic degree of 150,000 (Figure S6), a sufficiently high value for the purposes of this study (Section S3; Bevis et al., 2016; Jeans, 1923).

We downsample gridded estimates of $\frac{dh}{dt}$ (Figure 1) to a lower resolution between 0.0025° (228 m) and 0.01° (1.11 km) to avoid the high computing costs of modeling elastic deformation with $\frac{dh}{dt}$ at its native 90 m resolution. Histograms in Figure 3 show how sampling $\frac{dh}{dt}$ of the Glacier Bay, Juneau, and Stikine Icefields is affected by the method of sampling (average, median, and nearest neighbor) and the sampling resolution. Compared to the $\frac{dh}{dt}$ at its native resolution, sampling using the average or median results in an overly positive $\frac{dh}{dt}$ distribution that is accompanied by modest improvements as the sampling resolution increases. Using the nearest neighbor sampling method, the $\frac{dh}{dt}$ distribution converges to the native-resolution $\frac{dh}{dt}$ distribution as the sampling resolution increases (Figure 3c). We therefore sample the $\frac{dh}{dt}$ using the nearest neighbor method to create 456,420 evenly spaced, nonoverlapping discs 0.0025° in diameter.

The collection of 0.0025° diameter discs is converted from ice thinning rates to mass change rates using a density of 850 kg m^{-3} (Huss, 2013) and scaled by a factor of $4/\pi$ to account for the missing volume
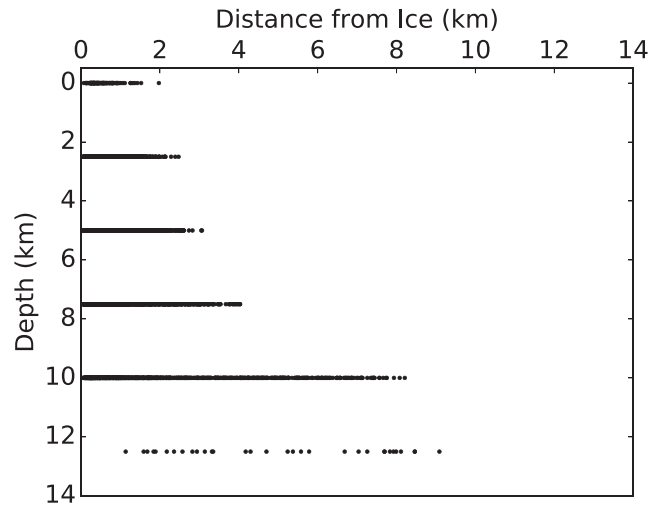
Figure 5. Depth of sensitivity to elastic structure (y axis) as a function of distance from the nearest ice-covered area. Pixels with a maximum difference less than 5% of the average GPS uncertainty (0.13 mm yr^{-1}) are omitted. Within 10-km distance from ice-covered areas, modeled elastic uplift rates are most sensitive to the upper 15 km of the elastic structure.

between each disc. The Green's function computation and convolution of the disc loads for the space-domain response are performed using the Regional ElAstic Rebound calculator (`REAR`; Melini et al., 2015) using the Legendre-domain load Love numbers computed using `giapy`. These steps are repeated after scaling all models for inelasticity using equation (1). We calculate the average of our elastic uplift rate ensemble ($\dot{\epsilon}_{LITHO}$) on a pixel-by-pixel basis as

$$\dot{\epsilon}_{LITHO}(x, y) = \frac{\sum_{i=1}^{N} \dot{\epsilon}_i(x, y)}{N}, \tag{2}$$

where N is 42. The uncertainties arising from modeling a heterogeneous elastic structure with a 1-D model ($\sigma_{\dot{\epsilon}}$) are found similarly by stacking all elastic uplift rate maps calculated from the LITHO1.0 models and taking the standard deviation of the elastic uplift rates at each pixel.

4. Results

4.1. Sensitivity to Elastic Structure With Depth
We construct sensitivity kernels to constrain the depth of the elastic structure to which the uplift signal is most sensitive following Doin et al. (2015) and Zhao et al. (2016). We divide the PREM elastic structure into 5-km-thick segments. The Young's modulus of the uppermost segment is reduced by a factor of 2, keeping the Poisson's ratio constant, and elastic uplift rates modeled from the perturbed structure are subtracted from those modeled with the original PREM. This process is repeated, each time migrating the perturbed layer down by a depth of 2.5 km until a depth of 120 km is reached.

Figure 4 shows a series of sensitivity kernels along a 12-km transect near the Grand Plateau Glacier in the Glacier Bay region (Figure 1). At the beginning of the transect, closest to the Grand Plateau Glacier, the largest increase in uplift rates results from a reduction in elastic parameters at 5-km depth, probing increasingly deep sections with greater distance along the transect. We consider amplitudes of the sensitivity kernel that are less than 5% of the average GPS uncertainty (0.13 mm yr^{-1}) to be insignificant, and the deepest portion of the elastic structure probed along this transect by the ice unloading is 10-km depth at a distance of 5 km from the Grand Plateau Glacier. A 1-D sampling of elastic structure sensitivity kernels is appropriate for this area because the Grand Plateau Glacier protrudes out slightly from the rest of the Glacier Bay region. Elsewhere, the ice geometry is more spatially complex, such as in between neighboring valley glaciers (e.g., the Grand Plateau and Fairweather glaciers; Figure 4), and requires 2-D information about the elastic structure sensitivity kernels. We calculate sensitivity kernels at 0.1° postings for all off-ice areas in the study region and record the depth and amplitude of the peak difference from the unperturbed model. A portion of this is shown as an example in Figures 4b and 4c. Pixels with amplitudes less than the 0.13-mm yr^{-1} threshold
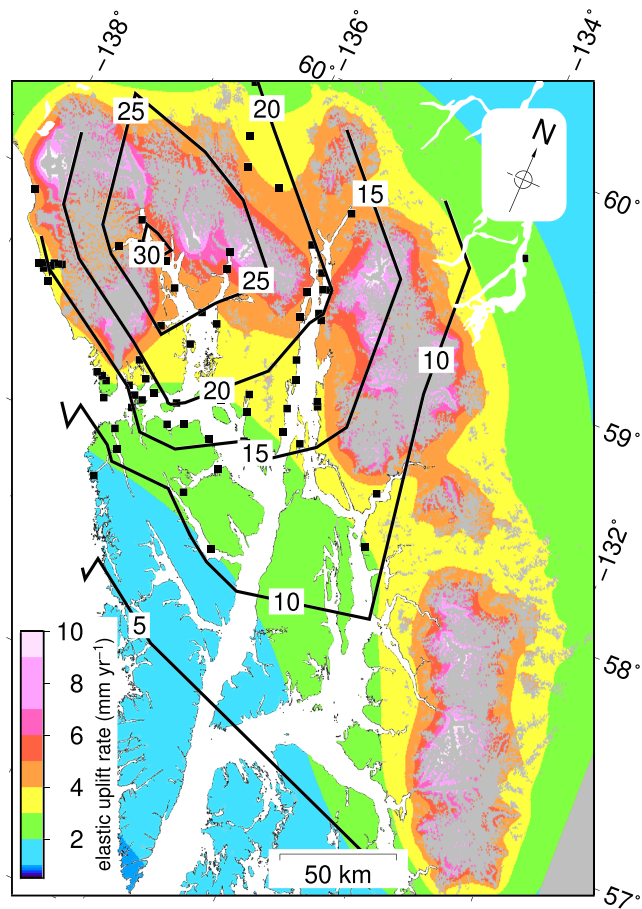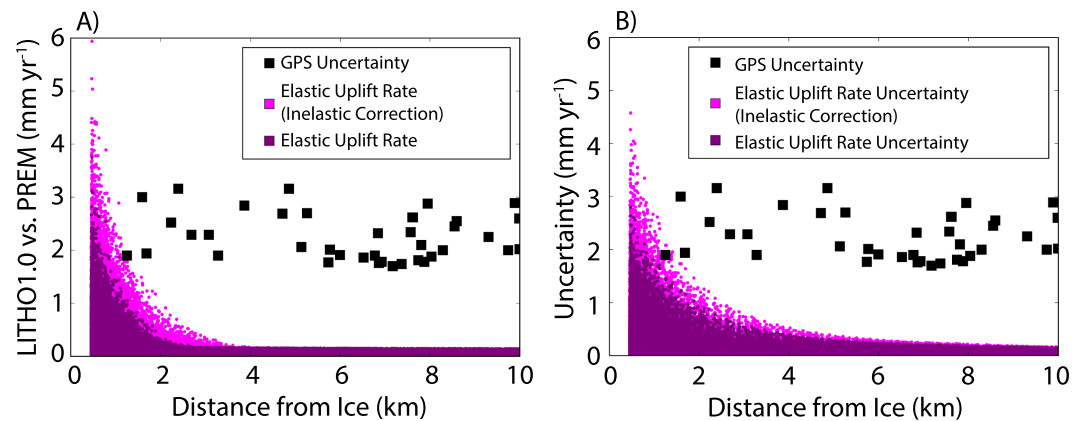
Figure 6. Average elastic uplift rates modeled using $\frac{dh}{dt}$ (Figure 1) and the ensemble of LITHO1.0 elastic structures (Figure 2) are shown in color. Differences between elastic uplift rates modeled using the Preliminary Reference Earth Model and those modeled using the ensemble of LITHO1.0 elastic structures are minor at this scale. Black lines show contoured uplift rates observed with campaign GPS (Elliott et al., 2010).

are removed, and the depth values are plotted against distance from the nearest ice-covered area (Figure 5). Figure 5 shows the depth of the elastic structures to which modeled uplift rates are most sensitive does not extend beyond 15 km below the surface. Since all LITHO1.0 elastic structures extend to a depth of at least 40 km, we are confident that all differences in elastic uplift rates are fully explored by our ensemble of elastic structures.

4.2. Sensitivity to Crustal Elastic Structure

Figure 6 shows the average of elastic uplift rates modeled for Southeast Alaska using estimated $\frac{dh}{dt}$ (Figure 1) and the ensemble of LITHO1.0 elastic structures, as well as the locations of campaign GPS observations (Elliott et al., 2010) and contoured observed total uplift rates. Differences in elastic uplift rates modeled using PREM and the LITHO1.0 ensemble are the most prominent in the near-field. To illustrate this, we plot these differences and elastic uplift rate uncertainty at every point in our study area against its distance from the nearest ice-covered area (Figure 7). At 500 m from ice-covered areas, or roughly two disc radii away from the center of the nearest load, the difference between $\dot{\epsilon}_{PREM}$ and $\dot{\epsilon}_{LITHO}$ is up to 2–4 mm yr^{-1}, or 1–2 times as large as the average uncertainty in the campaign GPS (Figure 7a). These differences decay quickly with distance from the ice. At 1 km away from the ice, differences between $\dot{\epsilon}_{PREM}$ and $\dot{\epsilon}_{LITHO}$ are 50% of the average GPS uncertainty (97% considering inelasticity) and become less than 10% at ~3.5 km away. The uncertainties of $\dot{\epsilon}_{LITHO}$ that result from lateral variations in the elastic structure (Figure 7b) show similar results. The uncertainties decay more slowly with distance from the ice and are 50% of the GPS uncertainty by 1.3 km (2.2 km with inelasticity), becoming less than 10% by 5 km. In Southeast Alaska, the vast majority of GPS observations were made beyond this distance and the choice of crustal elastic structure does not have

Figure 7. Scatter plots of all pixels of gridded elastic uplift rates plotted against distance to the nearest ice-covered area. (a) Difference between elastic uplift rates modeled using the LITHO1.0 ensemble ($\dot{\epsilon}_{\text{LITHO}}$) and those modeled using PREM ($\dot{\epsilon}_{\text{PREM}}$). (b) Uncertainty in elastic uplift rates due to lateral variations in crustal structure within the study region. The uncertainty of GPS observations are shown as black dots against distance from ice-covered areas. The lighter magenta color shows the impact of inelastic behavior in the crust on plots (a) and (b) found using equation (1). PREM = Preliminary Reference Earth Model.

a significant impact on the GIA deformation inferred. Using the PREM model, elastic uplift rates account for 18.8% of the total observed uplift, whereas this is $19.0 \pm 0.4\%$ if the LITHO1.0 elastic structures are used and $18.8 \pm 0.5\%$ after correcting for inelasticity.

Studies of glacial density or mass balance typically make use of geodetic observations close to the glacier of interest, as this is where the elastic deformation is the greatest (e.g., Bevan et al., 2015). To explore the sensitivity of these studies to the choice of crustal elastic structure, we consider only local differences from the global average elastic structure rather than lateral variations in elastic structure within the study region. Figure 8 shows the average increase in elastic uplift rates when modeled using local LITHO 1.0 elastic structure compared to elastic uplift rates modeled using PREM. Differences at 500 m from the ice peak at ~20% difference from $\dot{\epsilon}_{\text{PREM}}$ (dark color in Figure 8). When inelasticity is considered, this peaks at ~40%.

5. Discussion
5.1. Impact on Glacial Density and Mass Balance
Many studies that use GPS or interferometric synthetic aperture radar (InSAR) uplift observations to investigate dynamic glacier processes or glacier mass balance record the largest elastic uplift signal by taking
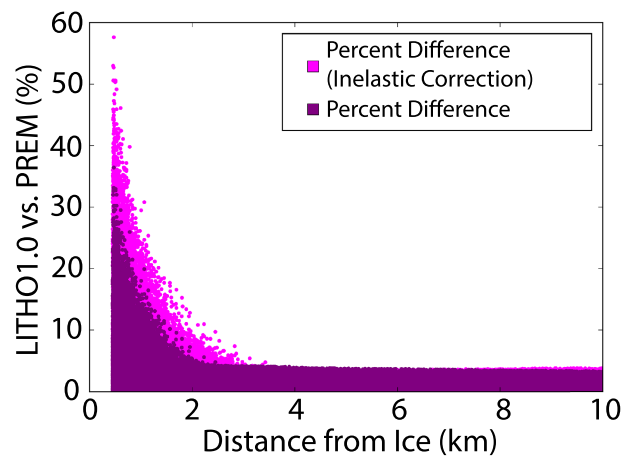
Figure 8. Scatter plot showing the percentage difference between elastic uplift rates modeled with local elastic structures and those modeled with PREM against distance from the nearest ice-covered area. The lighter magenta color shows the impact of inelastic behavior in the crust found using equation (1). PREM = Preliminary Reference Earth Model.

measurements close to the edge of the glacier (e.g., Adhikari et al., 2017; Bevan et al., 2015; Liu et al., 2012; Nielsen et al., 2013). This is also where the modeled elastic uplift rates are most sensitive to the local crustal elastic structure (Figures 4 and 7). Elastic uplift rates modeled with local crustal elastic structures are different from those modeled with PREM by up to ∼20% at the fastest thinning glaciers and as much as 40% if the effects of inelasticity are considered. This uncertainty range is pertinent to studies that use elastic uplift observations with volumetric constraints to estimate the density of glacier material lost or gained (e.g., Bevan et al., 2015), as the difference between the densities of firn (∼550 kg m^{-3}) and ice (900 kg m^{-3}) is comparable to the uncertainty range found here, particularly if inelasticity is considered.

In two studies of seasonal elastic deformation of Iceland, Drouin et al. (2016) and Compton et al. (2017) found that in order to match the known seasonal mass changes of the ice caps, it is necessary to scale the Green's functions of PREM by a factor of ∼2×. This difference is comparable to the 20–40% difference between $\dot{\epsilon}_{\mathrm{LITHO}}$ and $\dot{\epsilon}_{\mathrm{PREM}}$ found in this study (Figure 8); however, the differences seen here are significant only to <1 km from ice-covered areas. While some of the GPS observations used by Compton et al. (2017) are less than 1-km distance from the ice caps, most are greater than 10 km away. In Iceland, icecaps seasonally gain and lose ∼1.5–2.5 m w.e., representing much larger mass changes than the annual unloading in Southeast Alaska of ∼0.75 m w.e. yr^{-1} (Figure 1). The larger mass changes in Iceland seen seasonally could increase the distance from ice-covered areas to which deformation significantly depends on the site-specific elastic structure. While we find in this study that the elastic structure of the crust is important to consider for observations made <1 km from ice-covered areas, this distance threshold only applies to Southeast Alaska under the current annual mass loss rates. We recommend future investigations consider this distance sensitivity in other regions.

5.1.1. Inelasticity

In this study, we account for the effects of inelasticity in the upper crust using the empirical relations between the static-dynamic ratios of Young's moduli fit by Yale and Swami (2017) using and ensemble of triaxial strain experiments. In the absence of first principle methods for modeling inelasticity, these are a good first approximation. They suggest that the differences between the dynamic behavior of the crust at the time scales of seismic wave propagation compared to the static behavior at longer time scales could introduce significant bias and uncertainty in models of elastic deformation to cryospheric loads. The stress, strain, temperature conditions, and lithologies used in the experiments considered by Yale and Swami (2017) were designed to model the conditions of hydrocarbon reservoirs, and further experiments are needed to test how applicable these results are to a broader array of environmental conditions. The workflow presented in this study could be used to identify which areas are expected to have the greatest sensitivity to inelastic processes so that geodetic observations could be placed to optimize such experiments.

5.2. Impact on Inferred GIA

In Southeast Alaska, the majority of current GPS observations are located 5 km or more away from ice-covered areas. At these locations, the difference in modeled elastic uplift rates induced by modifying the crustal structure is insignificant compared to the campaign GPS uncertainty and does not affect interpretations of GIA deformation in the region made by previous studies (Elliott et al., 2010; Larsen et al., 2005; Sato et al., 2011). Based on these findings, we expect that in studies of other regions of rapid regional GIA (e.g., Iceland (Auriac et al., 2013), Patagonia (Lange et al., 2014), and regions of West Antarctica (Barletta et al., 2018; Nield et al., 2014), most of the geodetic observations will be similarly unaffected. However, among these areas are a few measurements where elastic uplift accounts for ≥30% of the observed uplift rates (e.g., near the head of Viedma and Upsala glaciers in the Southern Patagonian Icefield (Lange et al., 2014), Foyn Point in the Northern Antarctic Peninsula (Nield et al., 2014), and near the Backer Islands in the Amundsen Sea Embayment (Barletta et al., 2018)), and it is possible that these observations may be significantly impacted by their site-specific crustal structure.

We have also incrementally updated previous Southeast Alaska GIA studies by estimating the elastic deformation using ice mass balance estimated from satellite imagery that is roughly coterminous with the GPS acquisition time period. Using the updated ice mass balance estimates, we find that the percentage of total observed uplift rates described by elastic deformation in Southeast Alaska is ∼19%, lower than the ∼26% found by Sato et al. (2011) and in closer agreement with the ∼20% found by Larsen et al. (2005). Using a two layer Earth model, Sato et al. (2011) found that increased elastic deformation rates (and therefore lower inferred viscous deformation rates), resulted in estimates of asthenospheric viscosity of $5.6^{+6.4}_{-1.6} \times 10^{18}$ Pa s,

roughly 1.5× higher than the $3.7^{+0.3}_{-0.7} \times 10^{18}$ Pa s found by Larsen et al. (2005). The better agreement between the percentage of total observed uplift rates described by elastic deformation between this study and Larsen et al. (2005) supports their lower estimates of asthenospheric viscosity.

We propose two main reasons why we find lower elastic uplift rates on average than Sato et al. (2011) despite using more recent, and in many places higher, ice thinning rates. The first is due to the methods used for downsampling maps of ice thinning rates in preparation for modeling elastic deformation. In previous studies of GIA in Southeast Alaska, ice thinning rates were downsampled using averaging windows of 0.18° (Elliott et al., 2010; Larsen et al., 2005) and 0.083° × 0.042° (Sato et al., 2011). When ice thinning rates of this study are downsampled by averaging at 0.01° resolution, the $\frac{dh}{dt}$ distribution becomes too narrowly centered around its mode, resulting in an overly negative mass balance (Figure 3). Similar results are found when using median and nearest neighbor sampling methods at this resolution (Figure 3). Using $\frac{dh}{dt}$ sampled at this resolution results in biased elastic uplift rates (Figure S7), and downsampling with an average sampling approach at lower resolutions likely biased the ice thinning rate distributions of the previous studies. When sampling the $\frac{dh}{dt}$ with the nearest neighbor method at 0.005° and 0.0025° resolutions, the elastic deformation estimates converge at a lower value. The second reason why we found elastic deformation comprises a smaller percentage of the total observed uplift in comparison to Sato et al. (2011) is due to differences in ice mass balance estimates. The ice mass balance estimates used by Sato et al. (2011) to model elastic deformation were based on an elevation time series in which the latest elevations were from the radar-based SRTM DEM. Because the SRTM DEM is a C-band radar product, it penetrates into the snow, firn, and ice, mapping out an elevation below the surface. Previously, this penetration depth had been undercorrected (Berthier et al., 2018), resulting in overly negative ice mass balance estimates from time series ending in the SRTM DEM. In this study, this penetration depth is corrected using the "linear extrapolation" method (Section S1.1; Berthier et al., 2016; Wang & Kääb, 2015). Ice thinning rates estimated from a combination of the SRTM and elevation data based on optical imagery agree well with our estimates of $\frac{dh}{dt}$ based solely on optical imagery (Figure S3), as well as with ice mass balance estimates from previous studies based on independent data sets (A. J. Johnson et al., 2013).

6. Conclusions

We quantify the uncertainties in modeled elastic uplift response of the solid Earth to deglaciation between the years 2000 and 2017 in Southeast Alaska. Using an ensemble of site-specific 1-D elastic structures, we account for differences between the properties of our study region and that of the global average (i.e., PREM), the effects of modeling a laterally variable region using 1-D elastic structures, and the inelastic behavior of the upper crust. Uncertainties associated with the choice of elastic structure dominate the elastic uplift rate uncertainty at locations close to ice-covered areas (i.e., less than ~1-km distance), where they can be 1–2× larger than the average campaign GPS uncertainty. Indeed, close to ice-covered areas, elastic uplift rates modeled using local elastic structures can have differences of up to 20–40% to those modeled using PREM. This has the potential to introduce large biases into glaciological studies that use observations of elastic uplift observations close to ice-covered areas, and we recommend that future studies use caution in considering the choice of elastic structure. These uncertainties are largely attenuated at distances greater than 1 km from ice-covered areas. The vast majority of GPS observations in this region of Southeast Alaska were made past this distance threshold, where elastic uplift rate uncertainties are small in comparison, and do not affect interpretations of GIA deformation made by previous studies. Differences in load changes could alter the distance from ice-covered areas to which deformation significantly depends on the site-specific elastic structure, and the 1-km distance threshold found in this study applies only to Southeast Alaska. We recommend further investigation into the impact of elastic uplift rate uncertainties in other deglaciating regions.

References

Adhikari, S., Ivins, E. R., & Larour, E. (2017). Mass transport waves amplified by intense Greenland melt and detected in solid Earth deformation. *Geophysical Research Letters*, *44*, 4965–4975. https://doi.org/10.1002/2017GL073478

Ameen, M. S., Smart, B. G. D., Somerville, J. Mc., Hammilton, S., & Naji, N. A. (2009). Predicting rock mechanical properties of carbonates from wireline logs (A case study: Arab-D reservoir, Ghawar field, Saudi Arabia). *Marine and Petroleum Geology*, *26*(4), 430–444.

Arendt, A. A., Echelmeyer, K. A., Harrison, W. D., Lingle, C. S., & Valentine, V. B. (2002). Rapid wastage of Alaska Glaciers and their contribution to rising sea level. *Science*, *297*, 382–386.

Asef, M. R., & Najibi, A. R. (2013). The effect of confining pressure on elastic wave velocities and dynamic to static Young's modulus ratio. *Geophysics*, *78*(3), D135–D142.

Auriac, A., Spaans, K. H., Sigmundsson, F., Hooper, A., Schmidt, P., & Lund, B. (2013). Iceland rising: Solid Earth response to ice retreat inferred from satellite radar interferometry and visoelastic modeling. *Journal of Geophysical Research: Solid Earth*, *118*, 1331–1344. https://doi.org/10.1002/jgrb.50082

Barletta, V. R., Bevis, M., Smith, B. E., Wilson, T., Brown, A., Bordoni, A., et al. (2018). Observed rapid bedrock uplift in Amundsen Sea embayment promotes ice-sheet stability. *Science*, *360*(6395), 1335–1339.

Berthier, E., Cabot, V., Vincent, C., & Six, D. (2016). Decadal region-wide and glacier-wide mass balances derived from multi-temporal ASTER satellite digital elevation models. Validation over the Mont-Blanc Area. *Frontiers in Earth Science*, *4*, 1–16. https://doi.org/10.3389/feart.2016.00063

Berthier, E., Larsen, C., Durkin, W. J., Willis, M. J., & Pritchard, M. E. (2018). Brief communication: Unabated wastage of the Juneau and Stikine icefields (Southeast Alaska) in the early 21st century. *The Cryosphere*, *12*(4), 1523–1530.

Bevan, S. L., Luckman, A., Khan, S. A., & Murray, T. (2015). Seasonal dynamic thinning at Helheim Glacier. *Earth and Planetary Science Letters*, *415*, 47–53. https://doi.org/10.1016/j.epsl.2015.01.031

Bevis, M., Melini, D., & Spada, G. (2016). On computing the geoelastic response to a disk load. *Geophysical Journal International*, *205*(3), 1804–1812.

Brantut, N., Heap, M. J., Meredith, P. G., & Baud, P. (2013). Time-dependent cracking and brittle creep in crustal rocks: A review. *Journal of Structural Geology*, *52*, 17–43.

Carcione, J. M., Poletto, F., & Farina, B. (2018). The burgers/squirt-flow seismic model of the crust and mantle. *Physics of the Earth and Planetary Interiors*, *274*, 14–22.

Cathles, L. M. (1975). *The Viscosity of the Earth's Mantle*. Princeton, NJ: Princeton University Press.

Cheng, C. H., & Johnston, D. H. (1981). Dynamic and static moduli. *Geophysical Research Letters*, *8*(1), 39–42.

Compton, K., Bennett, R. A., & Hreinsdóttir, S. (2015). Climate-driven vertical acceleration of Icelandic crust measured by continuous GPS geodesy. *Geophysical Research Letters*, *42*, 743–750. https://doi.org/10.1002/2014GL062446

Compton, K., Bennett, R. A., Hreinsdóttir, S., van Dam, T., Bordoni, A., Barletta, V., & Spada, G. (2017). Short-term variations of Icelandic ice cap mass inferred from cGPS coordinate time series. *Geochemistry, Geophysics, Geosystems*, *18*, 2099–2119. https://doi.org/10.1002/2017GC006831

Dehecq, A., Millan, R., Berthier, E., Gourmelen, N., Trouvé, E., & Vionnet, V. (2016). Elevation changes inferred from TanDEM-X data over the Mont-Blanc area: Impact of the X-band interferometric bias. *IEEE Journal of Selected Topics in Applied Earth Observations and Remote Sensing*, *9*(8), 3870–3882.

Dill, R., Klemann, V., Martinec, Z., & Tesauro, M. (2015). Applying local Green's functions to study the influence of the crustal structure on hydrological loading displacements. *Journal of Geodynamics*, *88*, 14–22.

Doin, M. P., Twardzik, C., Ducret, G., Lasserre, C., Guillaso, S., & Jianbao, S. (2015). InSAR measurement of the deformation around Siling Co Lake: Inferences on the lower crust viscosity in central Tibet. *Journal of Geophysical Research: Solid Earth*, *120*, 5290–5310. https://doi.org/10.1002/2014JB011768

Drouin, V., Heki, K., Sigmundsson, F., Hreinsdóttir, S., & Ófeigsson, B. G. (2016). Constraints on seasonal load variations and regional rigidity from continuous GPS measurements in Iceland, 1997-2014. *Geophysical Journal International*, *205*(3), 1843–1858.

Dziewonski, A. M., & Anderson, D. L. (1981). Preliminary reference Earth model. *Physics of the Earth and Planetary Interiors*, *25*(4), 297–356.

Elliott, J. L., Larsen, C. F., Freymueller, J. T., & Motyka, R. J. (2010). Tectonic block motion and glacial isostatic adjustment in Southeast Alaska and adjacent Canada constrained by GPS measurements. *Journal of Geophysical Research*, *115*, B09407. https://doi.org/10.1029/2009JB007139

Farrell, W. E. (1972). Deformation of the Earth by surface loads. *Reviews of Geophysics*, *10*(3), 761–797.

Gardelle, J., Berthier, E., & Arnaud, Y. (2012). Slight mass gain of Karakoram glaciers in the early twenty-first century slight mass gain of Karakoram glaciers in the early twenty-first century. *Nature Geoscience*, *5*(5), 1–4. https://doi.org/10.1038/ngeo1450

Gardner, A. S., Moholdt, G., Cogley, J. G., Wouters, B., Arendt, A. A., Wahr, J., et al. (2013). A reconciled estimate of glacier contributions to sea level rise: 2003 to 2009. *Science*, *340*(6134), 852–857.

Huss, M. (2013). Density assumptions for converting geodetic glacier volume change to mass change. *The Cryosphere*, *7*(3), 877–887.

Jeans, J. H. (1923). The propagation of earthquake waves. *Proceedings of the Royal Society A*, *102*(718), 554–574.

Johnson, A. J., Larsen, C. F., Murphy, N., Arendt, A. A., & Lee Zirnheld, S. (2013). Mass balance in the Glacier Bay area of Alaska, USA, and British Columbia, Canada, 1995-2011, using airborne laser altimetry. *Journal of Glaciology*, *59*(216), 632–648.

Johnson, P., & Rasolofosaon, P. (1996). Manifestation of nonlinear elasticity in rock: Convincing evidence over large frequency and strain intervals from laboratory studies. *Nonlinear Processes in Geophysics*, *3*(2), 77–88.

Kachuck, S. (2018). Time-domain glacial isostatic adjustment: Theory, computation, and statistical applications (Ph.D. Thesis).

Khan, S. A., Wahr, J., Stearns, L. A., Hamilton, G. S., van Dam, T., Larson, K. M., & Francis, O. (2007). Elastic uplift in southeast Greenland due to rapid ice mass loss. *Geophysical Research Letters*, *34*, L21701. https://doi.org/10.1029/2007GL031468

King, M. S. (1983). Static and dynamic elastic properties of igneous and metamorphic rocks from the Canadian shield.

Lange, H., Casassa, G., Ivins, E. R., Schröder, L., Fritsche, M., Richter, A., et al. (2014). Observed crustal uplift near the Southern Patagonian Icefield constrains improved viscoelastic Earth models, *41*, 805–812.

Larsen, C. F., Burgess, E., Arendt, A. A., O'Neel, S., Johnson, A. J., & Kienholz, C. (2015). Surface melt dominates Alaska glacier mass balance. *Geophysical Research Letters*, *42*, 5902–5908. https://doi.org/10.1002/2015GL064349

Larsen, C. F., Motyka, R. J., Arendt, A. A., Echelmeyer, K. A., & Geissler, P. E. (2007). Glacier changes in Southeast Alaska and northwest British Columbia and contribution to sea level rise. *Journal of Geophysical Research*, *112*, F01007. https://doi.org/10.1029/2006JF000586

Larsen, C. F., Motyka, R. J., Freymueller, J. T., Echelmeyer, K. A., & Ivins, E. R. (2005). Rapid viscoelastic uplift in Southeast Alaska caused by post-Little Ice Age glacial retreat. *Earth and Planetary Science Letters*, *237*(3-4), 548–560. https://doi.org/10.1016/j.epsl.2005.06.032

Liu, L., Wahr, J., Howat, I., Khan, S. A., Joughin, I., & Furuya, M. (2012). Constraining ice mass loss from Jakobshavn Isbræ (Greenland) using InSAR measured crustal uplift. *Geophysical Journal International*, *188*(3), 994–1006. https://doi.org/10.1111/j.1365-246X.2011.05317.x

Luthcke, S. B., Sabaka, T., Loomis, B., Arendt, A., McCarthy, J., & Camp, J. (2013). Antarctica, Greenland and Gulf of Alaska land-ice evolution from an iterated GRACE global mascon solution. *Journal of Glaciology*, *59*(216), 613–631.

Melini, D., Gegout, P., Midi-Pyrenees, O., & Spada, G. (2015). A regional elastic rebound calculator.

Melkonian, A. K., Willis, M. J., & Pritchard, M. E. (2016). Stikine icefield mass loss between 2000 and 2013/2014. *Frontiers in Earth Science*, *4*, 89.

Melkonian, A. K., Willis, M. J., Pritchard, M. E., Rivera, A., Bown, F., & Bernstein, S. A. (2014). Satellite-derived volume loss rates and glacier speeds for the Cordillera Darwin Icefield, Chile. *Cryosphere*, *7*(3), 823–839.

Moratto, Z. M., Broxton, M. J., Beyer, R. A., Lundy, M., & Husmann, K. (2010). Ames Stereo Pipeline, NASA's open source automated stereogrammetry software. In *Lunar and planetary science conference*, *41*, pp. 2364.

Najibi, A. R., Ghafoori, M., Lashkaripour, G. R., & Asef, M. R. (2015). Empirical relations between strength and static and dynamic elastic properties of Asmari and Sarvak limestones, two main oil reservoirs in Iran. *Journal of Petroleum Science and Engineering*, *126*, 78–82.

Nield, G. A., Barletta, V. R., Bordoni, A., King, M. A., Whitehouse, P. L., Clarke, P. J., et al. (2014). Rapid bedrock uplift in the Antarctic Peninsula explained by viscoelastic response to recent ice unloading. *Earth and Planetary Science Letters*, *397*, 32–41. https://doi.org/10.1016/j.epsl.2014.04.019

Nield, G. A., Whitehouse, P. L., King, M. A., & Clarke, P. J. (2016). Glacial isostatic adjustment in response to changing Late Holocene behaviour of ice streams on the Siple Coast, West Antarctica. *Geophysical Supplements to the Monthly Notices of the Royal Astronomical Society*, *205*(1), 1–21.

Nielsen, K., Khan, S. A., Spada, G., Wahr, J., Bevis, M., Liu, L., & van Dam, T. (2013). Vertical and horizontal surface displacements near jakobshavn isbræ driven by melt-induced and dynamic ice loss. *Journal of Geophysical Research: Solid Earth*, *118*, 1837–1844. https://doi.org/10.1002/jgrb.50145

Noh, M. J., & Howat, I. M. (2015). Automated stereo-photogrammetric DEM generation at high latitudes: Surface Extraction with TIN-based Search-space Minimization (SETSM) validation and demonstration over glaciated regions. *GIScience and Remote Sensing*, *52*(2), 198–217. https://doi.org/10.1080/15481603.2015.1008621

Nuimura, T., Fujita, K., Yamaguchi, S., & Sharma, R. R. (2012). Elevation changes of glaciers revealed by multitemporal digital elevation models calibrated by GPS survey in the Khumbu region, Nepal Himalaya, 1992-2008. *Journal of Glaciology*, *58*(210), 648–656.

Pan, E., Chen, J. Y., Bevis, M., Bordoni, A., Barletta, V. R., & Molavi Tabrizi, A (2015). An analytical solution for the elastic response to surface loads imposed on a layered, transversely isotropic and self-gravitating earth. *Geophysical Supplements to the Monthly Notices of the Royal Astronomical Society*, *203*(3), 2150–2181.

Pasyanos, M. E., Masters, T. G., Laske, G., & Ma, Z. (2014). LITHO1.0: An updated crust and lithospheric model of the Earth. *Journal of Geophysical Research: Solid Earth*, *119*, 2153–2173. https://doi.org/10.1002/2013JB010626

Pfeffer, W. T., Arendt, A. A., Bliss, A., Bolch, T., Cogley, J. G., Gardner, A. S., et al. (2014). The Randolph Glacier Inventory: A globally complete inventory of glaciers. *Journal of Glaciology*, *60*(221), 537–552.

Ramage, J. M., Isacks, B. L., & Miller, M. M. (2000). Radar glacier zones in Southeast Alaska, U.S.A.: Field and satellite observations. *Journal of Glaciology*, *46*(153), 287–296.

Sato, T., Larsen, C. F., Miura, S., Ohta, Y., Fujimoto, H., Sun, W., et al. (2011). Reevaluation of the viscoelastic and elastic responses to the past and present-day ice changes in Southeast Alaska. *Tectonophysics*, *511*(3-4), 79–88.

Sauber, J. M., & Molnia, B. F. (2004). Glacier ice mass fluctuations and fault instability in tectonically active Southern Alaska. *Global and Planetary Change*, *42*(1–4), 279–293.

Sella, G. F., Stein, S., Dixon, T. H., Craymer, M., James, T. S., Mazzotti, S., & Dokka, R. K. (2007). Observation of glacial isostatic adjustment in "stable" 700 North America with GPS. *Geophysical Research Letters*, *34*, L02306. https://doi.org/10.1029/2006GL027081

Shepherd, A., Ivins, E., Rignot, E., Smith, B., van den Broeke, M., Velicogna, I., et al. (2018). Mass balance of the Antarctic Ice Sheet from 1992 to 2017. *Nature*, *558*(7709), 219–222. https://doi.org/10.1038/s41586-018-0179-y

Smith, L. C., Forster, R. R., Isacks, B. L., & Hall, D. K. (1997). Seasonal climatic forcing of alpine glaciers revealed with orbital synthetic aperture radar. *Journal of Glaciology*, *43*(145), 480–488.

Spaans, K., Hreinsdóttir, S., Hooper, A., & Ó feigsson, B. G. (2015). Crustal movements due to Iceland's shrinking ice caps mimic magma inflow signal at Katla volcano. *Scientific Reports*, *5*, 10285. https://doi.org/10.1038/srep10285

Steffen, H., & Wu, P. (2011). Glacial isostatic adjustment in fennoscandiaa review of data and modeling. *Journal of Geodynamics*, *52*(3–4), 169–204.

Tesauro, M., Audet, P., Kaban, M. K, Bürgmann, R., & Cloetingh, S. (2012). The effective elastic thickness of the continental lithosphere: Comparison between rheological and inverse approaches. *Geochemistry, Geophysics, Geosystems*, *13*, Q09001. https://doi.org/10.1029/2012GC004162

Tutuncu, A. N., Podio, A. L., Gregory, A. R., & Sharma, M. M. (1998). Nonlinear viscoelastic behavior of sedimentary rocks, part I: Effect of frequency and strain amplitude. *Geophysics*, *63*(1), 184–194.

Wahr, J., Khan, S. A., Dam, T., Liu, L., Angelen, J. H., Broeke, M. R., & Meertens, C. M. (2013). The use of GPS horizontals for loading studies, with applications to Northern California and Southeast Greenland. *Journal of Geophysical Research: Solid Earth*, *118*, 1795–1806. https://doi.org/10.1002/jgrb.50104

Wang, D., & Kääb, A. (2015). Modeling glacier elevation change from DEM time series. *Remote Sensing*, *7*(8), 10117–10142. https://doi.org/10.3390/rs70810117

Willis, M. J., Melkonian, A. K., Pritchard, M. E., & Rivera, A. (2012). Ice loss from the Southern Patagonian Ice Field, South America, between 2000 and 2012. *Geophysical research letters*, *39*, L17501. https://doi.org/10.1029/2012GL053136

Wong, T.-F., & Baud, P. (2012). The brittle-ductile transition in porous rock: A review. *Journal of Structural Geology*, *44*, 25–53.

Yale, D. P., & Swami, V. (2017). Conversion of dynamic mechanical property calculations to static values for geomechanical modeling. *American Rock Mechanics Association*, 17–0644.

Zhao, W., Amelung, F., Dixon, T. H., Wdowinski, S., & Malservisi, R. (2014). A method for estimating ice mass loss from relative InSAR observations: Application to the Vatnajökull ice cap, Iceland. *Geochemistry, Geophysics, Geosystems*, *15*, 108–120. https://doi.org/10.1002/2013GC004936

Zhao, W., Amelung, F., Doin, M. P., Dixon, T. H., Wdowinski, S., & Lin, G. (2016). InSAR observations of lake loading at Yangzhuoyong Lake, Tibet: Constraints on crustal elasticity. *Earth and Planetary Science Letters*, *449*, 240–245. https://doi.org/10.1016/j.epsl.2016.05.044

Erratum

In the originally published version of this article, there were errors in Table 1 and throughout the text. These errors have been corrected, and this version may be considered the authoritative version of record.